# Scintillation Properties and Electronic Structures of the Intrinsic and Extrinsic Mixed Elpasolites $Cs_2NaRBr_3I_3$ ($R$ = La, Y)

Hua Wei,[1,*] Mao-Hua Du,[2] Luis Stand,[1] Zhao Zhao,[3] Hongliang Shi,[2] Mariya Zhuravleva,[1] and Charles L. Melcher[1]

[1]*Department of Materials Science and Engineering, Scintillation Materials Research Center, University of Tennessee, Knoxville, Tennessee 37996, USA*

[2]*Advanced Materials Group, Materials Science and Technology Division, Oak Ridge National Laboratory, Oak Ridge, Tennessee 37831, USA*

[3]*Department of Physics, Stanford University, Stanford, California 94305, USA*

(Received 15 July 2015; revised manuscript received 22 November 2015; published 19 February 2016)

Scintillators attract wide research interest for their distinct applications in radiation detection. Elpasolite halides are among the most promising scintillators due to their high structural symmetry and good scintillation performance. A better understanding of their underlying scintillation mechanism opens up possibilities in scintillator development. In this work, we employ a variety of experimental techniques to study the two mixed-anion elpasolites $Cs_2NaRBr_3I_3$ ($R$ = La, Y). The emission of intrinsic $Cs_2NaRBr_3I_3$ with a light yield ranging from 20 000 to 40 000 ph/MeV is dominant by self-trapped exciton emission. Partial substitution of $R$ with Ce introduces a competing emission, the $Ce^{3+}$ $5d$-to-$4f$ radiative transition. *Ab initio* calculations are performed to investigate the electronic structures as well as the binding energies of polarons in $Cs_2NaRBr_6$. The calculated large self-trapped exciton binding energies are consistent with the observed high light yield due to self-trapped exciton (STE) emission. The unique electronic structure of halide elpasolites as calculated enhances the STE stability and the STE emission. The highly tunable scintillation properties of mixed-anion elpasolites underscore the role of their complex scintillation mechanism. Our study provides guidance for the design of elpasolite scintillators with exceptional energy resolution and light yield desirable for applications.

DOI: 10.1103/PhysRevApplied.5.024008

## I. INTRODUCTION

Scintillators absorb and convert high-energy photons or particles into multiple low-energy photons [1]. They are widely used for x-ray, gamma-ray, neutron, and charged-particle detection. Positron emission tomography (PET), a state-of-the-art nuclear imaging tool to examine body metabolism for early-stage cancer diagnosis [2], has its ultimate performance strongly tied to the properties of scintillators [3–5]. LSO ($Lu_2SiO_5$:Ce) or its analogue LYSO [6] are currently employed in PET. However, the imaging quality suffers most from their low light yield. Besides, the shortage of the raw material $Lu_2O_3$ and the substantial increase of cost urge the industry to seek better performance scintillators with less cost. In high-energy physics, scintillators with fast timing and high density are desirable for designing next-generation hadron colliders [7]. In oil well logging, scintillators are used to measure the radioactivity of the clay formation as well as conduct the elemental analysis. The workhorse NaI:Tl is replaced by $LaBr_3$:Ce, which yields more precise data with a shorter response time [8].

Over the past few decades, halide compounds have shown great potential as next-generation scintillators [4,9–11]. For instance, $LaBr_3$:Ce achieves a state-of-the-art coincidence-resolving time of 100 ps for time-of-flight PET [12]. $KSr_2I_5$:Eu possesses an exceptional energy resolution of 2.4% at 662 keV [13]. $Cs_2LiYCl_6$:Ce has efficient neutron or gamma-ray pulse shape discrimination ability for nuclear nonproliferation applications [14]. Among the numerous metal halides, elpasolite halides with highly symmetric crystal structures are of particular interest [15–18]. Their cubic or pseudocubic isotropic structures reduce the impact of thermomechanical stress during crystal growth and, thus, minimize the cracks and improve the production yields [19].

The discovery of elpasolite halides can be tracked back to 1883, where $K_2NaAlF_6$ was first identified in minerals [20]. Since then, numerous elpasolites have been reported. The halide elpasolites have a general form of $A_2BRX_6$, where $A$ and $B$ are monovalent alkali metals, $R$ is a trivalent rare-earth element, and $X$ is the halogen element. The elpasolite structure can be viewed as a cationic-ordered perovskite ($CaTiO_3$-type) structure [21]. In the ideal situation, the elpasolite structure has $Fm\bar{3}m$ cubic symmetry.

*Present address: Radiation Monitoring Devices Inc., 44 Hunt Street, Watertown, MA, 02472, USA.
sundyhw@gmail.com

 

According to Goldschmidt [22,23], the Goldschmidt tolerance factor of elpasolites can be expressed as

$$t = \frac{R_A + R_X}{\sqrt{2}[\frac{1}{2}(R_B + R_R) + R_X]}, \quad (1)$$

where $t$ represents the Goldschmidt tolerance factor and $R_A$, $R_B$, $R_R$, and $R_X$ are the ionic radii of $A^+$, $B^+$, $R^{3+}$, and $X^-$, respectively.

Based on Eq. (1), for the mixed-anion system in this work, the Goldschmidt tolerance factor can be written as

$$t = \frac{R_A + \overline{R_X + R_{X'}}}{\sqrt{2}[\frac{1}{2}(R_B + R_R) + \overline{R_X + R_{X'}}]}, \quad (2)$$

where $R_X + R_{X'}$ is the average ionic radius of the two halogen anions $X^-$ and $X'^-$. As the tolerance factor approaches unity, the crystal structure is more likely to be cubic [21,23,24].

Doty *et al.* [25] consider 640 potential halide elpasolites as scintillation host materials. Among the large number of elpasolites, only a few of them have been experimentally proved as scintillators. $Cs_2LiYCl_6$:Ce is one of the elpasolite scintillators successfully applied in neutron and gamma-ray detection [15,26]. $Cs_2LiYCl_6$:Ce has a cubic crystal structure with a band gap of 6.8–7.5 eV [27]. The light yield for gamma-ray excitation is around 20 000 ph/MeV. $Cs_2LiYBr_6$:Ce is reported to have the same crystal structure, but with a smaller band gap of 5.7 eV and a higher light yield of 25 000 ph/MeV [28]. Similar Li-containing elpasolite scintillators including $Cs_2LiLaCl_6$:Ce, $Cs_2LiLaBr_6$:Ce [26], $Cs_2LiLaCl_6$:Ce [29], and $Cs_2LiCeBr_6$ [30] are reported elsewhere. Besides the Li-containing elpasolite scintillators, non-Li-containing halide elpasolites are also reported as promising scintillators, such as $Cs_2LiCeBr_6$ [31], $Cs_2NaGdBr_6$:Ce [32], and $Cs_2NaLaI_6$:Ce [33].

Among all the reported halide elpasolite scintillators, none showed a light yield exceeding 50 000 ph/MeV. The highest record is 50 000 ph/MeV ($^{137}$Cs source) for $Cs_2LiLaBr_6$:Ce with optimized Ce concentration [34]. A recent theoretical work on the rare-earth chloride elpasolites by Shi and Du [35] shows that (i) the localized $d$ or $f$ states of the trivalent rare earth form the conduction-band edge, while the large distance between the trivalent cations in the double-perovskite structure further localizes these states, and (ii) the localized Cl $3p$ states make up the valence band, which is narrow with small dispersion. The narrow conduction and valence bands favor charge localization, resulting in inefficient carrier mobility to the activators such as $Ce^{3+}$. Less electronegative halogens, i.e., Br and I, should enhance cross-band-gap hybridization and lead to more efficient carrier (holes, in particular) transport.

However, a larger ionic radius of $Br^-$ or $I^-$ lowers the Goldschmidt tolerance factor [Eq. (1)] and can potentially lead to low symmetry structure. According to Zhou and Doty's [25,36] predictions on cubic halide elpasolites with the embedded-ion method, a cubic lattice can experience a symmetry breaking or structural distortion, i.e., from cubic to tetragonal, when the Goldschmidt tolerance factor is lowered to 0.909. Here, the calculated Goldschmidt tolerance factor of $Cs_2NaLaBr_3I_3$ and $Cs_2NaYBr_3I_3$ is 0.902 and 0.921, respectively.

For the elpasolite-bearing low-symmetry crystal structures, such an anisotropic structure and the solid-solid phase transition could prevent us from obtaining high-quality single crystals. As a matter of fact, we fail to obtain $Cs_2NaLaI_6$ and $Cs_2NaYI_6$ single crystals during our multiple trials for crystal growth. The as-grown polycrystals contain low-symmetry phases and have poor scintillation performance.

In the previous work, we proposed an approach to engineer the halide elpasolite scintillators by mixing halogen anions of iodine and bromine [37]. This method has two main advantages: (i) the iodine with less electronegativity improves the charge-carrier mobility efficiency; (ii) more importantly, the partial mixing can still maintain cubic or nearly cubic crystal symmetry; i.e., $Cs_2NaYBr_3I_3$ and $Cs_2NaLaBr_3I_3$ preserve the cubic and tetragonal structure, respectively. The gamma-ray light yield of $Cs_2NaLaBr_3I_3$: 5% Ce (by mole) is 58 000 ph/MeV. Moreover, an excellent energy resolution of 2.9% at 662 keV is achieved in a small specimen. The light yield and energy resolution are better than both end-point elpasolites of the Br-I solid solution. $Cs_2NaYBr_3I_3$: 2% Ce has an energy resolution of 3.3% at 662 keV and a light yield of 43 000 ph/MeV [37].

The aim of this work is to investigate the origins of the scintillation emission in two intrinsic and extrinsic (Ce-doped) mixed-anion elpasolites. The joint experimental and theoretical study indicates the potential of developing intrinsic scintillators with high light yield based on self-trapped exciton (STE) emission at room temperature (RT). A variety of experimental techniques are employed to measure their spectroscopic and scintillation response at different temperatures. Electronic structures of the non-mixed elpasolite are calculated, as well as the binding energy of electron and hole polarons and STEs. The results indicate that the unique electronic structure and the large binding energies of the STE are stable at RT. Therefore, the stable STE leads to the scintillation emission of the intrinsic mixed elpasolite, which is rarely observed in other metal halides at RT.

Furthermore, the method of anion mixing can be applied to improve the scintillation properties and broaden the use of elpasolite crystals in radiation-detection applications.

## II. EXPERIMENTAL AND THEORETICAL METHODS

### A. Single crystal growth

Single crystals of intrinsic $Cs_2NaYBr_3I_3$ and $Cs_2NaLaBr_3I_3$ and extrinsic $Cs_2NaYBr_3I_3$:Ce and $Cs_2NaLaBr_3I_3$:Ce with various Ce concentrations (by mole) are grown by the Bridgman method. All the Ce-doped samples in this work are referred to as extrinsic samples. All the starting materials are 4 N pure anhydrous materials purchased from Sigma Aldrich. In order to drive out the residual oxygen and moisture, the starting materials are baked in a vertical clamshell furnace under vacuum ($10^{-6}$ torr) at 250 °C for 6–15 h before melting. Iodine in the mixed-anion elpasolite comes from CsI and NaI. Then the starting materials are melted and mixed by the multiple alternating direction method [38–40]. The furnace is programmed with two zones: a hot zone at the top and a cold zone at the bottom. The pulling rate is approximately 3 mm/h, and the cooling rate is 3°–5° C/h. Single crystals 8–15 mm in diameter are successfully obtained. Figure 1 shows a crystal boule of $Cs_2NaYBr_3I_3$:Ce during growth and after growth, as well as the crystal structure of a cubic mixed-anion elpasolite.

Inductively coupled plasma optical emission spectroscopy (ICP-OES) (Optima 2100 by PerkinElmer®) is utilized to detect the concentration of $Ce^{3+}$. The instrument detection limit is 1 ppm. All the intrinsic crystal samples are dissolved in DI water. The standard cerium ICP reference solution is used.

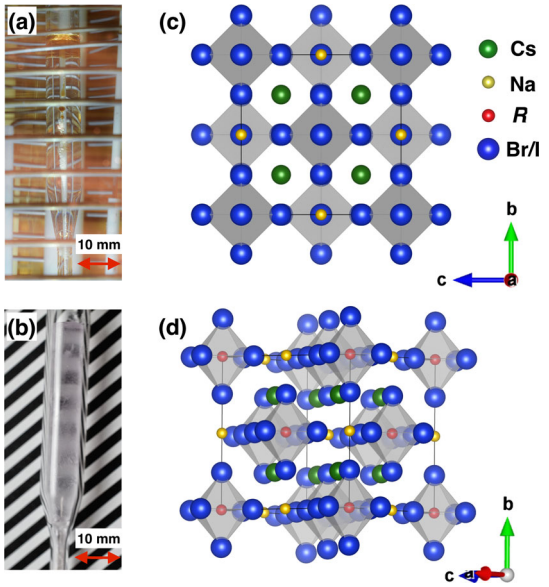


FIG. 1. (a) The crystal is grown in a gold-coated transparent furnace and (b) a transparent crystal boule of $Cs_2NaYBr_3I_3$: 2% Ce; (c),(d) the cubic crystal structure of mixed-anion elpasolite viewed from two perspectives. The drawings in (c) and (d) are produced using Visualization for Electronic and Structure Analysis (vesta) software [41].

### B. Scintillation properties

Radioluminescence (RL) spectra are recorded at RT by exciting the samples with x rays from a CMX-003 x-ray generator. The target material is Cu. The voltage and current of the x-ray tube are 35 kV and 0.1 mA, respectively. The emission spectra are recorded with a 150-mm focal length monochromator (PI ACTON SpectraPro SP-2155m) over a wavelength range of 200–800 nm. The aperture of the incident light is at the maximum. The experimental geometry is the standard reflection mode, and most of the radiation interaction occurs near the surface of the crystal [42].

The scintillation decay time is measured at RT with the time-correlated single-photon counting technique [43]. The photomultiplier tubes (PMTs) used for the start and stop signals are both Hamamatsu R2059. An Ortec 556 High Voltage Power Supply (HVPS) is set to −1700 V. The measurement range is 10 $\mu$s. The irradiation source is $^{137}$Cs. The sample is next to the start PMT and 4.5 inches away from the stop PMT. All the scintillation time curves are fit by exponential decay functions.

The scintillation light yield is measured by coupling a sample to the PMT to record the pulse height spectra. A Hamamatsu R6321-100 PMT is used for the energy-resolution calculation because of its high quantum efficiency, and a calibrated Hamamatsu R3177-50 with detailed quantum efficiency at each wavelength (200–700 nm) is used for the absolute value of light yield. A $^{137}$Cs gamma-ray source is used in the measurement. A Canberra 2005 pre-amp and an Ortec 672 spectroscopy amplifier with a shaping time of 10 $\mu$s amplifies and shapes the PMT signal. An Ortec 556 HVPS is set to −1600 V for PMT R3177-50 and −1000 V for R6321-100, respectively. A multiple channel analyzer (Tukan 8 K) is used to histogram the pulses [44]. A Spectralon hemispherical dome is used to reflect the scintillation light into the PMT. The sample is put into a quartz vial filled with mineral oil, which is used to protect the sample from moisture. The total light loss due to the vial is approximately 10%.

### C. Optical properties

Photoluminescence (PL) emission and excitation spectra are measured with a Horiba Jobin Yvon Fluorolog 3 Spectrofluorometer equipped with a 450-W Xe lamp. Horiba Jobin Yvon NanoLED light sources with various wavelengths are used for photoluminescence decay measurement; the pulse duration is less than 1 ns, and the repetition rate of the LED is set to 1 MHz. A Hamamatsu R928 PMT is used to record the emission as a function wavelength. The sample is protected in a vacuum-tight sample holder with a transparent quartz window. A closed-cycle compressed helium cryostat (Advanced Research Systems, DE-202) is used to cool and heat the sample from 40 to 750 K under vacuum ($< 10^{-3}$ torr). The cooling

and heating rate is set to 9 K/ min and controlled by a Lakeshore 332 Temperature Controller.

### D. Computational method

Density-functional calculations are performed to study the electronic structure and carrier self-trapping in $Cs_2NaLaBr_6$, $Cs_2NaYBr_6$, $Cs_2NaLaI_6$, and $Cs_2NaYI_6$ [45,46]. PBE0 hybrid functionals [47], which incorporate 25% Hartree-Fock exchange, are used to calculate band structures and energetics of small polaron STE. The use of hybrid functionals provides an improved description of band gaps, defects, and charge localization associated with the formation of small polarons and STE [48–51]. It is difficult to simulate a random alloy. We simply arrange the Br and I ions such that, within each $MBr_3I_3$ ($M$ = Na or La/Y) octahedron, there is a threefold symmetry.

The electron-ion interactions are described using projector-augmented-wave potentials [52,53]. The valence wave functions are expanded on a plane-wave basis with a cutoff energy of 260 eV. Experimental lattice constants are used for all elpasolites. Atomic coordinates are optimized by minimizing the Feynman-Hellmann forces to below 0.05 eV/Å.

The charge transition level $\varepsilon(q/q')$, induced by Ce impurity or polarons, is determined by the Fermi level ($\varepsilon_F$) at which the formation energies of the impurity or defect with charge states $q$ and $q'$ are equal to each other. $\varepsilon(q/q')$ can be calculated using

$$\varepsilon\left(\frac{q}{q'}\right) = \frac{E_{D,q'} - E_{D,q}}{q - q'}, \tag{3}$$

where $E_{D,q}$ ($E_{D,q'}$) is the total energy of the supercell that contains the relaxed structure of a defect at charge state $q$ ($q'$).

The binding energies of hole and electron polarons (or the energies of hole and electron polarons relative to those of a free hole and free electron) are $\varepsilon_{\text{hole-pol}}(+/0)$-$\varepsilon_v$ and $\varepsilon_c - \varepsilon_{\text{electron-pol}}(0/-)$, respectively. Here, $\varepsilon_v$ and $\varepsilon_c$ are the energies of the valence-band maximum (VBM) and the conduction-band minimum (CBM), respectively.

## III. RESULTS

### A. RL spectra

The RL emission spectra comparison of both intrinsic and extrinsic $Cs_2NaLaBr_3I_3$ and $Cs_2NaYBr_3I_3$ at RT is shown in Fig. 2. The intrinsic samples have a broader emission peak compared with the extrinsic samples, which can be attributed to the STE emission. Such broad emissions are also observed in other halide elpasolites RL spectra [15,28,54]. The STE emissions in the extrinsic samples are vaguely shown; this indicates a good energy transfer from the host to the $Ce^{3+}$ ions.

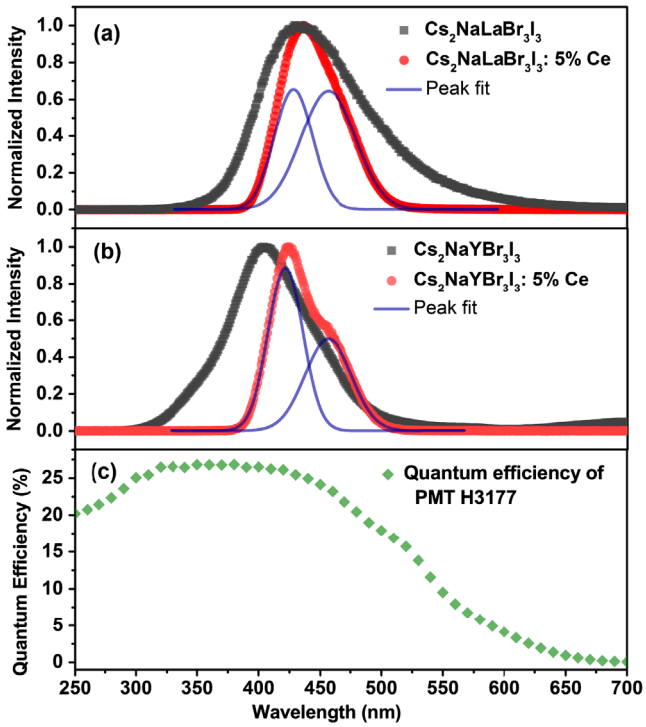


FIG. 2. RL spectra comparison of intrinsic and extrinsic samples of (a) $Cs_2NaLaBr_3I_3$ and (b) $Cs_2NaYBr_3I_3$. The emission peaks of the extrinsic samples are fit with a Gaussian function, as shown in the blue curves. The data are normalized by the maximum peak intensity. (c) The quantum efficiency curve of a common PMT (Hamamatsu H3177-50). The spectra of extrinsic samples $Cs_2NaLaBr_3I_3$ and $Cs_2NaYBr_3I_3$ are adapted from Ref. [37].

It is worth noting that the emission peak of the extrinsic samples looks asymmetric where there are two close peaks [the splitting in Fig. 2(b) is more visible]. These two peaks originate from the split ground states $4f$ ($^2F_{5/2}$) and $4f$ ($^2F_{7/2}$) of $Ce^{3+}$.

The quantum efficiency curve of a common PMT (Hamamatsu H3177-50) is shown in Fig. 2(c). One can see the emission of both the intrinsic and extrinsic scintillators matches well with the highly efficient detection region of the PMT. This guarantees high photon-detection efficiency during measurements.

### B. PL spectra

The PL excitation and emission spectra of extrinsic and intrinsic $Cs_2NaLaBr_3I_3$ at 40 K are shown in Figs. 3 and 4. In the PL excitation spectra of both extrinsic and intrinsic $Cs_2NaLaBr_3I_3$, an isolated excitation band is observed from 250 (4.96 eV) to 280 nm (4.43 eV) in the shadowed regions of Figs. 3(a) and 3(b) [55]. Compared with the extrinsic $Cs_2NaLaBr_3I_3$, this excitation band is much stronger in intrinsic $Cs_2NaLaBr_3I_3$. It is ascribed to an exciton-excitation band located slightly below the conduction band for electrons [56]. The ionized electron is not

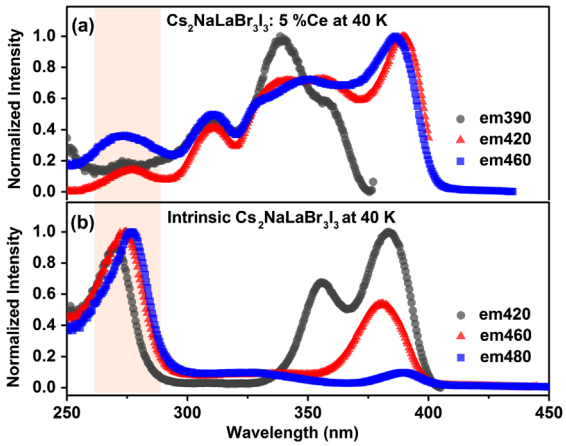


FIG. 3. PL excitation spectra at 40 K of (a) $Cs_2NaLaBr_3I_3$: 5% Ce and (b) intrinsic $Cs_2NaLaBr_3I_3$. Both spectra are normalized to the maximum peak. Excitation spectra are monitored at various emission wavelengths. The highlighted region from 250 to 280 nm indicates the strong exciton-excitation band in intrinsic samples.

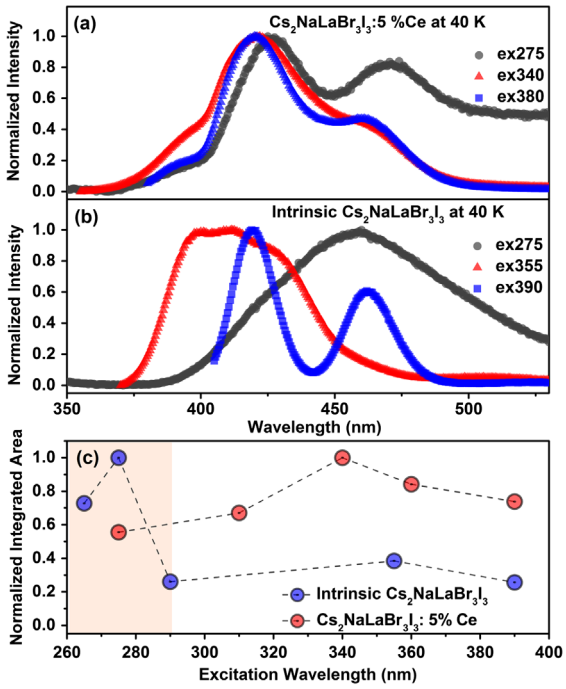


FIG. 4. PL emission spectra at 40 K of (a) $Cs_2NaLaBr_3I_3$: 5% Ce and (b) intrinsic $Cs_2NaLaBr_3I_3$. Both spectra are normalized to the maximum peak. (c) The integrated emission spectra under different excitation wavelengths of intrinsic $Cs_2NaLaBr_3I_3$ (blue dot) and extrinsic $Cs_2NaLaBr_3I_3$: 5% Ce (red dot), respectively. The integration range is from 350 to 550 nm. The integrated intensity is calculated with the un-normalized raw data. The raw intensity comparison without normalization can be found in Supplemental Material [55]. The intrinsic sample gives strong emission intensity under the exciton excitation at a shorter wavelength.

free to move and could not reach the conduction band. Notice that the exciton-band energy can be determined by the optical absorption and transmittance measurement, where it could be extrapolated from the fundamental absorption edge [37]. In addition, the broad excitation band from 310 to 405 nm is assigned to the splitting of $Ce^{3+}$ $5d$ states.

In the emission spectra of $Cs_2NaLaBr_3I_3$ : Ce in Fig. 4(a), the splitting of Ce-$4f$ levels is well resolved. The intense 420- and 460-nm emission peaks are attributed to the transition from the $Ce^{3+}$ $5d$ state to the split ground states of $4f$ ($^2F_{5/2}$) and $4f$ ($^2F_{7/2}$). Such emissions are observed when the excitation falls in the $Ce^{3+}$ excitation band (310–405 nm). However, when excited with 275 nm, the emission peak becomes broader, although the $Ce^{3+}$ $4f$-splitting feature can still be seen. This emission possibly comes from a combination of STE emission and $Ce^{3+}$ emission. In the intrinsic $Cs_2NaLaBr_3I_3$ as shown in Fig. 4(b), the $Ce^{3+}$ emission is also observed at 420 and 460 nm. This is probably due to the trace amount of Ce contamination in the sample, even though ICP-OES does not detect any $Ce^{3+}$ ions. When the nominal intrinsic $Cs_2NaLaBr_3I_3$ is excited at 275 nm, the emission is broad, and no resolved $Ce^{3+}$ emission is observed comparing with the extrinsic elpasolites. This indicates that STE emission dominates in the intrinsic samples, while STE is suppressed with $Ce^{3+}$ doping.

The integrated PL emission intensity of both intrinsic $Cs_2NaLaBr_3I_3$ and $Cs_2NaLaBr_3I_3$: 5% Ce at different excitation wavelengths is shown in Fig. 4(c). The integration is from 350 to 550 nm. For the intrinsic sample, the emission intensity is much more intense when the excitation falls in the exciton-excitation band, which again indicates the STE dominates in the intrinsic samples. In the Ce-doped sample, the change of the integrated emission intensity is more stable, and the value is slightly higher when the excitation falls in the $Ce^{3+}$ $4f-5d$ excitation band.

Similar behaviors are also observed in extrinsic and intrinsic $Cs_2NaYBr_3I_3$, as shown in Figs. 5 and 6. In the excitation spectra in Fig. 5, the long-wavelength excitation bandwidth of the Ce-doped sample is larger than the intrinsic sample. The feature of an exciton-excitation band is observed in both samples. In the emission spectra of intrinsic $Cs_2NaYBr_3I_3$ in Fig. 6(a), when excited with a shorter wavelength of 273 nm, a distinct broader long-wavelength emission peak occurs, comparing with the well-defined Ce-doped emission in Fig. 6(b).

Figure 7 shows the intrinsic $Cs_2NaYBr_3I_3$ PL spectra at RT for comparison. Different from the 40-K excitation spectra, the short-wavelength exciton-excitation band (250–280 nm) is enhanced with elevated temperature compared with the $Ce^{3+}$ excitation band (330–410 nm). Based on the emission spectra in Fig. 7(b), the STE-induced emission ranges broadly from 320 to 550 nm, and it is similar to its RL emission spectrum. On the other hand, the $Ce^{3+}$ excitation band overlaps with the broad STE

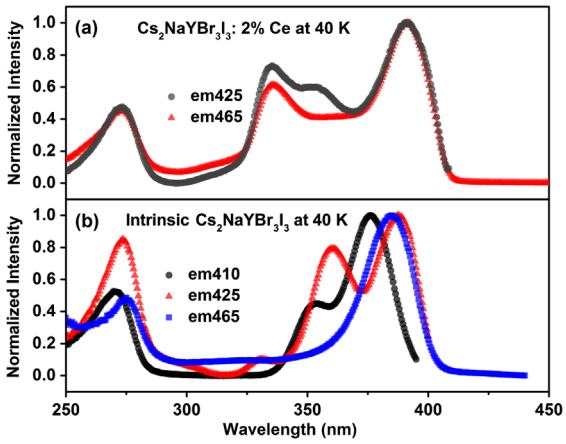


FIG. 5. PL excitation spectra at 40 K of (a) $Cs_2NaYBr_3I_3$: 5% Ce and (b) intrinsic $Cs_2NaYBr_3I_3$. Both spectra are normalized to the maximum peak.

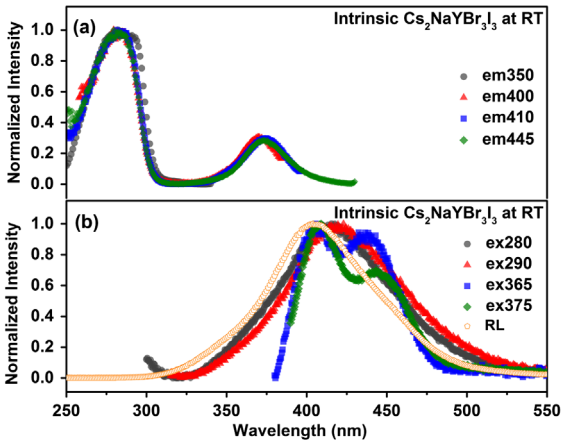


FIG. 7. (a) PL excitation and (b) PL emission spectra of intrinsic $Cs_2NaYBr_3I_3$ at RT; the RL spectrum of $Cs_2NaYBr_3I_3$ at RT is also plotted for comparison.

emission band, and this can result in radiative transfer from STE to $Ce^{3+}$; i.e., the STE emission can be absorbed at the $Ce^{3+}$ site which reemits photons [28].

### C. PL kinetics

The PL decay times of both extrinsic and intrinsic $Cs_2NaLaBr_3I_3$ and $Cs_2NaYBr_3I_3$ are recorded at different temperatures. For extrinsic $Cs_2NaLaBr_3I_3$ and $Cs_2NaYBr_3I_3$, the exciton-excitation wavelengths of 295 nm and the $Ce^{3+}$ excitation wavelength of 370 nm are chosen, respectively, in order to monitor the emissions from STE and $Ce^{3+}$. From the PL spectra in Figs. 3–6, one can see that the STE and $Ce^{3+}$ emissions have a broad overlap between 320 and 550 nm. To reveal the excitation spectra of both STE and $Ce^{3+}$, the emission at 420 nm is monitored. Unfortunately, for intrinsic $Cs_2NaLaBr_3I_3$ and $Cs_2NaYBr_3I_3$, when using an airtight sample holder on the cryogenic station for a low-temperature measurement, the emission is too weak to observe when excited at 295 nm. Instead, the RT PL decay curves are shown here to illustrate the kinetics of exciton-excitation-induced emission. The instrumental response decay curve is also plotted for reference. All the PL decay-fitting parameters are shown in Table I.

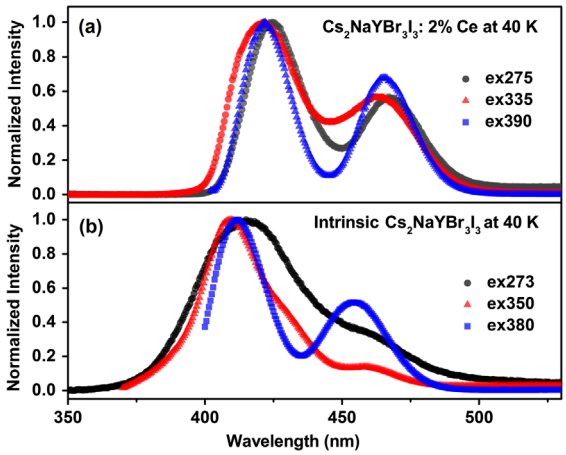


FIG.6. PL emission spectra at 40 K of (a) $Cs_2NaYBr_3I_3$: 5% Ce and (b) intrinsic $Cs_2NaYBr_3I_3$. Both spectra are normalized to the maximum peak.

In Figs. 8(a) and 9(a), for both extrinsic $Cs_2NaLaBr_3I_3$ and $Cs_2NaYBr_3I_3$ at 40 K, when exciting with 333 and 370 nm, the PL decay time is around 30 ns. Both of the excitation wavelengths belong to the $Ce^{3+}$ excitation band; therefore, the PL decay can be ascribed to the $Ce^{3+}$ characteristic $5d$-$4f$ transition. When exciting with 295 nm, which falls into the exciton-excitation band, the PL decay monitored at 420 nm is also around 30 ns. It is clearly seen that the 295-nm-excited emission creates much higher background than the 370-nm-excited fast emission. This reveals the existence of a much longer decay component [57]. Considering the excitation wavelength of 295 nm falls in the exciton-excitation band, it is reasonable that the excitation at 295 nm creates the excitons that have a long lifetime at the microsecond level, which is prominently longer than the direct electron-hole capture of $Ce^{3+}$.

The PL decay of intrinsic samples is shown in Figs. 8(b) and 8(c) and 9(b) and 9(c). When exciting with 370 nm and monitoring at 420 nm, both $Cs_2NaLaBr_3I_3$ and $Cs_2NaYBr_3I_3$ show a 30-ns characteristic fast $Ce^{3+}$ decay, similar to the extrinsic samples. This is due to the trace amount of $Ce^{3+}$ in the nominal intrinsic samples. When monitoring the 420-nm emission with 295-nm excitation, which belongs to the exciton-excitation band, the long decay time above 1 $\mu$s is observed. It is readily ascribed to the characteristic STE decay [23,26-29,54].

For the mixed elpasolites, the $Ce^{3+}$ has a fast PL decay time of around 30 ns, while the STE has a longer decay time of more than 1 $\mu$s. Because of the domination of $Ce^{3+}$ in the emission, only in the intrinsic sample can the

TABLE I. The PL decay fitting parameters of intrinsic and extrinsic $Cs_2NaLaBr_3I_3/Cs_2NaYBr_3I_3$ at various emission and excitation wavelengths and temperatures.

| | PL decay parameters (ns) | | |
|---|---|---|---|
| | ex295 em 420 | ex 33 em 420 | ex370 em420 |
| $Cs_2NaLaBr_3I_3$: 5% Ceat 40 K | $29.76 \pm 0.21$ | $38.01 \pm 0.07$ | $37.42 \pm 0.10$ |
| Intrinsic $Cs_2NaLaBr_3I_3$ at 40 K | | | $24.83 \pm 0.03$ |
| Intrinsic $Cs_2NaLaBr_3I_3$ at RT | $32.19 \pm 1.67$ (16%)$1055.87 \pm 71.89$ (84%) | | $23.91 \pm 0.03$ |
| $Cs_2NaYBr_3I_3$: 2% Ceat 40 K | $30.93 \pm 0.17$ | $29.35 \pm 0.05$ | $32.55 \pm 0.07$ |
| Intrinsic $Cs_2NaYBr_3I_3$ at 40 K | | | $22.49 \pm 0.02$ |
| Intrinsic $Cs_2NaYBr_3I_3$ at RT | $31.89 \pm 0.24$ (5%)$813.78 \pm 120$ (95%) | | $20.47 \pm 0.03$ |

STE decay be recorded distinctively. This indicates the competition between STE and $Ce^{3+}$ in the scintillation process: (i) The STE transfers its energy to $Ce^{3+}$ radiatively, which means $Ce^{3+}$ is absorbing the emission from STE. In this case, the decay time of $Ce^{3+}$ emission should be equivalent to or slightly slower than the decay time of STE. (ii) The STE transfers its energy to $Ce^{3+}$ nonradiatively by thermal-activated diffusion. In this case, the time constant should be relatively close to the characteristic decay time of $Ce^{3+}$. One would also expect an increase of $Ce^{3+}$ emission intensity as the temperature increases before reaching thermal quenching.

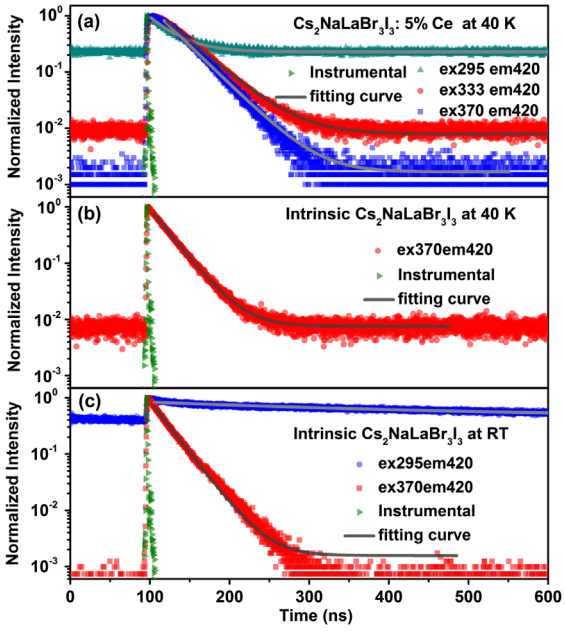


FIG. 8. (a) PL decay of $Cs_2NaLaBr_3I_3$: 5% Ce at 40 K: The emission at 420 nm is monitored with excitation wavelengths of 295, 333, and 370 nm. The instrumental response is measured to be less than 1 ns, which can be ignored in the decay fitting. The PL decay curves are fit with a single decay exponential function. PL decay of intrinsic $Cs_2NaLaBr_3I_3$ at (b) 40 K and (c) RT. The emission at 420 nm is monitored with excitation wavelengths of 295 and 370 nm. The emission cannot be detected with 295-nm excitation in the 40-K measurement, because the cryogenic sample holder blocks the weak emission.

### D. Scintillation kinetics

The scintillation decay between intrinsic and extrinsic samples at RT is compared in Figs. 10(a) and 10(b). The decay curves of extrinsic and intrinsic $Cs_2NaLaBr_3I_3$ and $Cs_2NaYBr_3I_3$ are fit with three and two exponential decay functions, respectively. The decay time and the ratio are shown in the inset tables.

The fast-decay component below 100 ns is a characteristic of the $Ce^{3+}$ deexcitation process, and it is the major contribution in both extrinsic $Cs_2NaLaBr_3I_3$ and $Cs_2NaYBr_3I_3$. It is clearly seen that the fast-decay component is absent in the intrinsic samples. Instead,

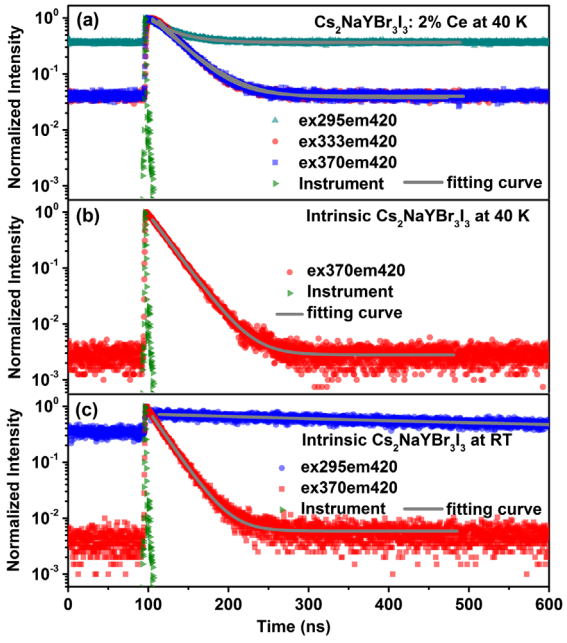


FIG. 9. (a) PL decay of $Cs_2NaYBr_3I_3$: 2% Ce at 40 K: The emission at 420 nm is monitored with excitation wavelengths of 295, 333, and 370 nm. The PL decay curves are fit with a single decay exponential function. PL decay of intrinsic $Cs_2NaYBr_3I_3$ at (b) 40 K and (c) RT. The emission at 420 nm is monitored with excitation wavelengths of 295 and 370 nm. The emission cannot be detected with 295-nm excitation in the 40-K measurement, because the cryogenic sample holder blocks the weak emission.

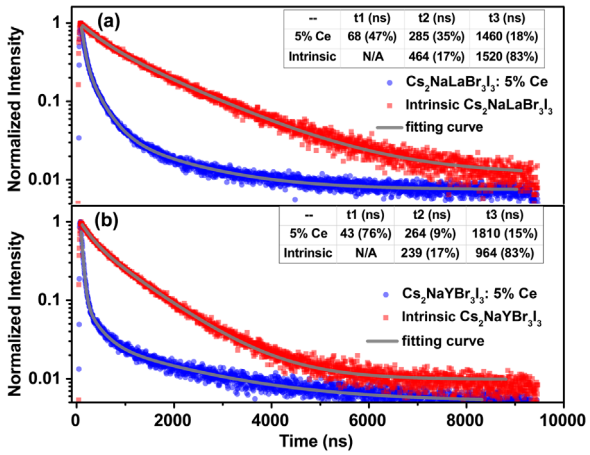


FIG. 10 Scintillation decay profiles of intrinsic and extrinsic samples of (a) $Cs_2NaLaBr_3I_3$ and (b) $Cs_2NaYBr_3I_3$. The extrinsic decay curves are fit with three decay exponential functions, and the intrinsic decay curves are fit with two decay exponential functions. The fitting curves are shown in solid gray lines. The scintillation rising time of the extrinsic $Cs_2NaLaBr_3I_3$ and $Cs_2NaYBr_3I_3$ can be found in Ref. [55].

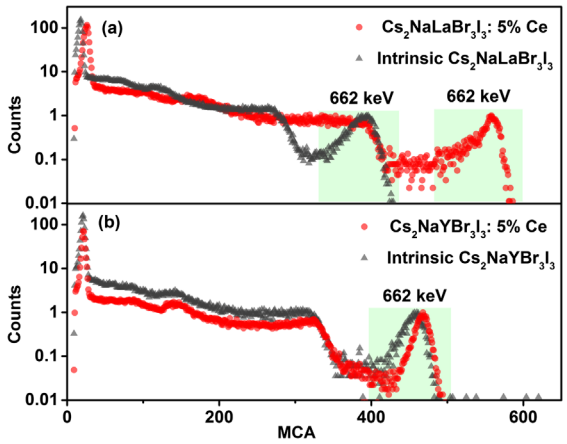


FIG. 11. Gamma-ray pulse height spectra of intrinsic and extrinsic samples of (a) $Cs_2NaLaBr_3I_3$ and (b) $Cs_2NaYBr_3I_3$. The photopeak at 662 keV is highlighted to better illustrate the position. Cs-137 source is used. The pulse height spectra of extrinsic samples $Cs_2NaLaBr_3I_3$ and $Cs_2NaYBr_3I_3$ are adapted from Ref. [37].

the slow-decay component around 1 $\mu$s contributes to more than 80% of the total emission in the intrinsic samples. In both intrinsic and extrinsic samples, this microsecond slow-decay component is observed and ascribed to STE. Combes *et al.* [15] and van't Spijker [58] suggest that, in the halide elpasolites, the creation of free electrons in the conduction band and free holes in the valence band is followed by the creation of self-trapped holes, i.e., a $V_k$ center. The formation of $V_k$ centers is common in halides due to the localized valence-band states and their soft lattice [59,60]. The self-trapped holes can trap free electrons to form self-trapped excitons, which will result in STE emission. The STE is thermally activated and can be quenched with elevated temperature. In most elpasolites, the STE can be formed at RT [15,29–31,54,61].

The intermediate-decay component of several hundred nanoseconds is observed in both intrinsic and extrinsic samples. However, this decay component is not observed in the PL decay measurement. It is not likely to be the direct deexcitation of $Ce^{3+}$. Compared to many other $Ce^{3+}$-doped elpasolite, this intermediate-decay component is commonly seen [15,29–31,54,61], yet no clear origin has been given at this point. One possible origin is the nonradiative energy transfer from STE to $Ce^{3+}$, and it is normally faster than the radiative transfer. Another possible reason can be related to the detrapped electrons from shallow traps.

### E. Scintillation light yield

The pulse height spectra of both intrinsic and extrinsic $Cs_2NaLaBr_3I_3$ and $Cs_2NaYBr_3I_3$ are shown in Figs. 11(a) and 11(b). For the extrinsic scintillators, the Ce concentration is optimized for a best energy resolution at 662 keV in our previous work [37]. Table II is a list of the light yields and energy resolutions for selected samples.

While the intrinsic samples have a lower light yield than the extrinsic samples, the intrinsic mixed elpasolites have a light yield comparable to NaI:Tl. In fact, their light yield is higher than many other well-known extrinsic scintillators, such as LSO:Ce [6], YAP:Ce [62], etc.

### F. First-principles calculation

The valence band of the rare-earth elpasolites studied here is made up of halogen $p$ states, while the conduction band is derived from the rare-earth $d$ states. The band structures of $Cs_2NaLaBr_6$ and $Cs_2NaYBr_6$ are shown in Fig. 12. Both valence and conduction bands are narrow, having small dispersion. Narrow valence bands are typical for halides.

However, the narrow conduction band is unusual and is related to the structure and chemistry of elpasolites [35,63,64]. In rare-earth elpasolites, such as $Cs_2NaYBr_6$, the rare-earth cation is much more electronegative than the alkali metal cations, and, as a result, the conduction band is mainly a rare-earth $d$ band, which is separated in energy from the alkali metal $s$ band. The large nearest-neighbor

TABLE II. Light yield and energy resolution comparison.

| | Light yield (ph/ MeV) | Energy resolution (662 keV) |
|---|---|---|
| Intrinsic $Cs_2NaLaBr_3I_3$ | 39 000 | 6.6% |
| $Cs_2NaLaBr_3I_3$: 5%Ce | 58 000 | 2.9% |
| Intrinsic $Cs_2NaYBr_3I_3$ | 40 000 | 4.3% |
| $Cs_2NaYBr_3I_3$: 2%Ce | 43 000 | 3.3% |

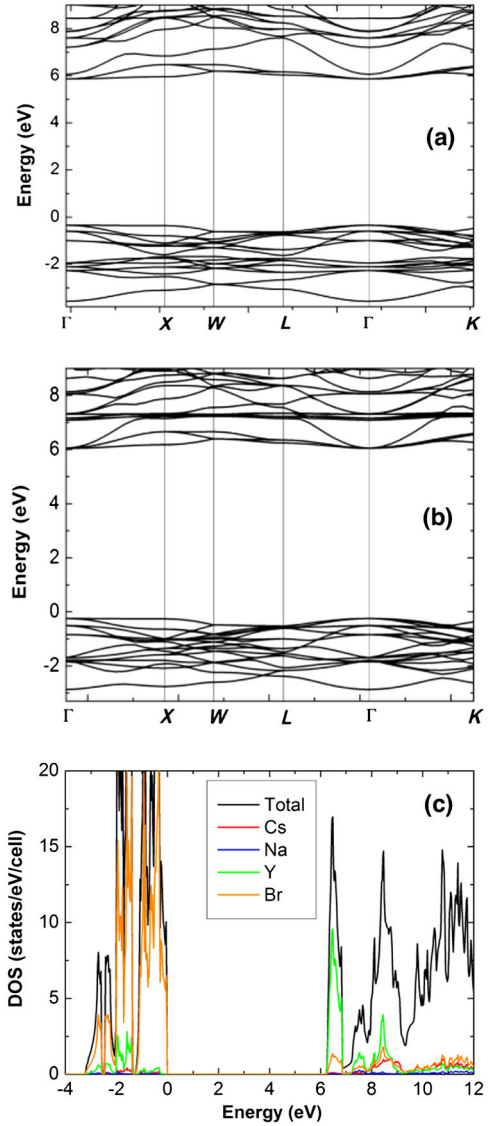


FIG. 12. Band structure of (a) $Cs_2NaLaBr_6$ and (b) $Cs_2NaYBr_6$; (c) density of states (DOS) of $Cs_2NaYBr_6$.

distance between the rare-earth cations leads to weak coupling between the rare-earth $d$ orbitals and, consequently, a very narrow conduction band as seen in Figs. 12(a) and 12(b).

The band gaps of $Cs_2NaLaBr_6$ and $Cs_2NaYBr_6$ calculated using PBE0 hybrid functionals are 6.31 and 6.25 eV, respectively. Mixing bromides with iodides in a 1:1 ratio reduces the band gaps to 5.41 and 5.15 eV for $Cs_2NaLaBr_3I_3$ and $Cs_2NaYBr_3I_3$, respectively, in agreement with experimentally measured band gaps of 4.92 and 4.87 eV, respectively. Pure iodides (i.e., $Cs_2NaLaI_6$ and $Cs_2NaYI_6$) are not synthesized. We optimize the lattice constants of $Cs_2NaLaI_6$ and $Cs_2NaYI_6$ in cubic structures and calculate the band gaps. Note that the structures of iodides are likely not cubic. The purpose of the calculations is to have a rough idea of the band gaps of iodides.

TABLE III. Calculated binding energies (in eV) of small hole and electron polarons and STE in $Cs_2NaLaBr_6$ and $Cs_2NaYBr_6$.

| | Hole polaron | Electron polaron | STE |
|---|---|---|---|
| $Cs_2NaLaBr_6$ | 0.63 | 0.47 | 0.42 |
| $Cs_2NaYBr_6$ | 0.51 | 0.39 | 0.36 |

The calculated band gaps of the hypothetical cubic $Cs_2NaLaI_6$ and $Cs_2NaYI_6$ are 5.02 and 4.93 eV, respectively. It therefore appears that mixing bromides and iodides in a 1:1 ratio reduces the band gaps of the alloys substantially from those of bromides to very close to those of iodides. The substantial reduction of the band gap by alloying leads to a significant increase in the light yield as observed experimentally.

The narrow valence and conduction bands favor the self-trapping of both holes and electrons, forming small hole and electron polarons. The calculated binding energies of small hole and electron polarons and STEs in $Cs_2NaLaBr_6$ and $Cs_2NaYBr_6$ are shown in Table III. Note that the binding energy of a STE is calculated relative to the energies of small hole and electron polarons. The large binding energies shown in Table III show that STEs are stable at RT and could survive at even higher temperatures. As a result, STE emission should be observed at RT. The energy transfer in these elpasolites is due to hopping of localized STEs rather than the diffusion of free carriers. Therefore, the electron transfer is inefficient, which leads to a relatively slow scintillation decay as also observed experimentally.

Mixing bromides with iodides is expected to reduce the small hole binding energy and the STE binding energy, resulting in a somewhat faster energy transfer.

## IV. DISCUSSION

An energy diagram of $Cs_2NaLaBr_3I_3$:Ce and $Cs_2NaYBr_3I_3$:Ce is plotted in Fig. 13 based on the well-resolved PL excitation spectra and temperature-dependent PL decay time of $Ce^{3+}$ [55]. From the temperature-dependent photoluminescence kinetics measurement, it is found that the estimated $5d_1$ level is located more than 1 eV below the conduction band in both compounds. This region could potentially be occupied by electron traps. The trapped electrons can then be thermally detrapped with time constants related to the trap depths. Afterwards, the detrapped electron can recombine with a hole, which is previously trapped at the $Ce^{3+}$ site. This delayed process may cause the intermediate scintillation decay (a few hundred nanoseconds). Thermoluminescence studies are necessary to determine the lifetimes of the electron traps and potentially correlate them to the intermediate scintillation decay time.

Based on the PL decay and scintillation decay results, three scintillation mechanisms are proposed in the mixed-anion elpasolites, as shown in Fig. 14.

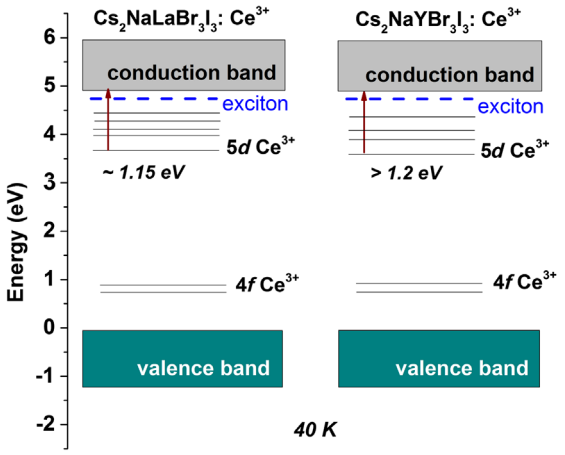


FIG. 13. Energy diagram of $Cs_2NaLaBr_3I_3$ (left) and $Cs_2NaYBr_3I_3$ (right) at 40 K.

(1) *Fast emission*.—After the initial ionization of free holes and electrons, the $Ce^{3+}$ luminescence centers sequentially capture holes from the valence band and then electrons from the conduction band and then deexcite via photon emission.
(2) *Intermediate emission*.—Shallow defects temporarily trap electrons during the electron thermalization stage. The trapped electrons can be de-trapped thermally and then migrate to $Ce^{3+}$ centers.
(3) *Slow emission*.—After a hole is created, it can be trapped by two anions in the valence band and form a $V_k$ center. The $V_k$ center can trap a free electron to form a STE. The STE is capable of radiative deexcitation and results in photon emission. The emitted photon can either escape from the crystal surface or be absorbed by $Ce^{3+}$ with subsequent reemission. Alternatively, the STE can migrate to a $Ce^{3+}$ site and transfer its energy to the $Ce^{3+}$ nonradiatively.

$Cs_2NaLaBr_3I_3$ and $Cs_2NaYBr_3I_3$ are discussed in this work. Furthermore, the established connection between the theoretical and experimental results on these two compounds can be developed as a predictive model on scintillator design. For instance, in the band engineering of elpasolite halides, the correlation between mixing anion and scintillation properties can be predicted: Less electronegative halogen is preferred until the distortion of lattice severely deteriorates the crystal quality (low transparency, cracks, secondary phase, etc.). Also, the cations can play an important role. They can change the crystal structure (e.g., $Cs_2NaLaBr_3I_3$ is cubic and $Cs_2NaYBr_3I_3$ is tetragonal), alter the conduction band edge (especially the trivalence cations), and eventually affect the scintillation properties.

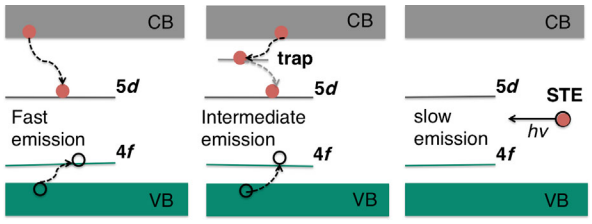


FIG. 14. Diagram of three different scintillation decay processes in the mixed elpasolite scintillators.

## V. CONCLUSIONS

The spectroscopic analyses and scintillation properties of intrinsic and extrinsic $Cs_2NaYBr_3I_3$ and $Cs_2NaLaBr_3I_3$ mixed-anion elpasolites are discussed. Compared with the intrinsic scintillators, the energy resolution (at 662 keV) of the extrinsic scintillators is improved by 56% and 23% for $Cs_2NaLaBr_3I_3$ and $Cs_2NaYBr_3I_3$, respectively. The PL excitation and emission spectra indicate that the exciton-excitation band is below the optical absorption edge, which results in a broad STE emission overlapping with the $Ce^{3+}$ emission. The PL decay time of the STE emission is about 1 $\mu$s compared with the 30-ns decay time of $Ce^{3+}$ 5*d*-4*f* transition at 40 K. *Ab initio* calculations performed on $Cs_2NaLaBr_6$ and $Cs_2NaYBr_6$ show their small dispersive conduction bands, which can lead to stable electron polarons at RT. The large binding energy of STE suggests its stability at RT and, thus, results in the scintillation emission directly from STE. The calculated large STE binding energies are consistent with the observed high light yield of the intrinsic samples due to STE emission. Mixing less electronegative iodine with bromine can effectively reduce the STE binding energy and band gap of the host materials. This could improve the energy transfer efficiency from STE to $Ce^{3+}$ in the extrinsic scintillators. Mixing anions of halide scintillators can be an effective approach to improve the performance of current in-use scintillators. Also, it can be used to design scintillators to meet the specific need in radiation-detection applications.

## ACKNOWLEDGMENTS

We thank Mr. Bo Bishop (University of Tennessee–Knoxville) for the technical support of making quartz ampoules and Dr. Pieter Dorenbos (Delft University of Technology) for the scientific discussions. M.-H. D. and H. S. are supported by the Department of Energy, Office of Science, Basic Energy Sciences, Materials Sciences and Engineering Division.

[1] G. F. Knoll, *Radiation Detection and Measurement*, 4th ed. (Wiley, New York 2010).
[2] L. Schrevens, N. Lorent, C. Dooms, and J. Vansteenkiste, The Role of PET scan in diagnosis, staging, and management of non-small cell lung cancer, Oncologist **9**, 633 (2004).

[3] L. E. Adam, J. S. Karp, M. E. Daube-Witherspoon, and R. J. Smith, Performance of a whole-body PET scanner using curve-plate NaI(Tl) detectors, J. Nucl. Med. **42**, 1821 (2001).

[4] C. L. Melcher, Scintillation crystals for PET, J. Nucl. Med. **41**, 1051 (2000).

[5] Y. Wu, F. Meng, Q. Li, M. Koschan, and C. L. Melcher, Role of $Ce^{4+}$ in the Scintillation Mechanism of Codoped $Gd_3Ga_3Al_2O_{12}:Ce$, Phys. Rev. Applied **2**, 044009 (2014).

[6] C. Melcher and J. Schweitzer, Cerium-doped lutetium oxyorthosilicate: A fast, efficient new scintillator, IEEE Trans. Nucl. Sci. **39**, 502 (1992).

[7] P. Lecoq and M. Korzhik, Scintillator developments for high energy physics and medical imaging, IEEE Trans. Nucl. Sci. **47**, 1311 (2000).

[8] C. L. Melcher, J. S. Schweitzer, R. A. Manente, and C. A. Peterson, Applications of single-crystals in oil-Well logging, J. Cryst. Growth **109**, 37 (1991).

[9] M. J. Weber, Scintillation: Mechanisms and new crystals, Nucl. Instrum. Methods Phys. Res., Sect. A **527**, 9 (2004).

[10] S. E. Derenzo, M. J. Weber, W. E. Bourret-Courchesne, and M. K. Klintenberg, The quest for the ideal inorganic scintillator, Nucl. Instrum. Methods Phys. Res., Sect. A **505**, 111 (2003).

[11] P. Dorenbos, Light output and energy resolution of $Ce^{3+}$-doped scintillators, Nucl. Instrum. Methods Phys. Res., Sect. A **486**, 208 (2002).

[12] R. S. Dennis, S. Stefan, V. Ruud, T. v. D. Herman, D. Peter, L. Herbert, and J. B. Freek, $LaBr_3:Ce$ and SiPMs for time-of-flight PET: Achieving 100 ps coincidence resolving time, Phys. Med. Biol. **55**, N179 (2010).

[13] L. Stand, M. Zhuravleva, H. Wei, and C. L. Melcher, Crystal growth and scintillation properties of potassium strontium bromide, Opt. Mater. **46**, 59 (2015).

[14] M. M. Bourne, C. Mussi, E. C. Miller, S. D. Clarke, S. A. Pozzi, and A. Gueorguiev, Characterization of the CLYC detector for neutron and photon detection, Nucl. Instrum. Methods Phys. Res., Sect. A **736**, 124 (2014).

[15] C. M. Combes, P. Dorenbos, C. W. E. van Eijk, K. W. Kramer, and H. U. Gudel, Optical and scintillation properties of pure and $Ce^{3+}$-doped $Cs_2LiYCl_6$ and $Li_3YCl_6:Ce^{3+}$ crystals, J. Lumin. **82**, 299 (1999).

[16] M. Laroche, M. Bettinelli, S. Girard, and R. Moncoge, f-d luminescence of $Pr^{3+}$ and $Ce^{3+}$ in the chloro-elpasolite $Cs_2NaYCl_6$, Chem. Phys. Lett. **311**, 167 (1999).

[17] P. A. Rodnyi, V. B. Mikhailik, G. B. Stryganyuk, A. S. Voloshinovskii, C. W. E. van Eijk, and G. F. Zimmerer, Luminescence properties of Ce-doped $Cs_2LiLaCl_6$ crystals, J. Lumin. **86**, 161 (2000).

[18] M. Zhuravleva, L. Stand, H. Wei, C. Hobbs, L. A. Boatner, J. O. Ramey, K. Shah, A. Burger, E. Rowe, P. Bhattacharya, E. Tupitsyn, and C. L. Melcher, in *Proceedings of the 2013 IEEE Nuclear Science Symposium and Medical Imaging Conference (NSS/MIC)* (IEEE, New York, 2013).

[19] K. O. Findley, J. Johnson, D. F. Bahr, F. P. Doty, and J. Frey, Fracture and deformation behavior of common and novel scintillating single crystals, in *Proceeding of SPIE 6707*, Penetrating Radiation Systems and Applications VIII (SPIE, San Diego, 2007), p. 670706.

[20] L. R. Morss, Crystal-structure of dipotassium sodium fluoroaluminate elpasolite, J. Inorg. Nucl. Chem. **36**, 3876 (1974).

[21] I. N. Flerov, M. V. Gorev, K. S. Aleksandrov, A. Tressaud, J. Grannec, and M. Couzi, Phase transitions in elpasolites (ordered perovskites), Mater. Sci. Eng. R **24**, 81 (1998).

[22] V. M. Goldschmidt, Die Gesetze der Krystallochemie, Naturwissenschaften **14**, 477 (1926).

[23] A. Gormezano and M. T. Weller, New quadruple perovskites $Ln_2Ba_2TixSn_{2-x}Cu_2O_{11}$ $(0 < X < 2)$-controlling copper-oxygen distances in potential superconducting parent phases, J. Mater. Chem. **3**, 979 (1993).

[24] F. Prokert and K. S. Aleksandrov, Neutron-scattering studies on phase-transition and phonon-dispersion in $Cs_2NaBiCl_6$, Phys. Status Solidi B **124**, 503 (1984).

[25] F. P. Doty, X. Zhou, P. Yang, and M. A. Rodriguez, report, Sandia National Lab, 2012.

[26] J. Glodo, E. van Loef, R. Hawrami, W. M. Higgins, A. Churilov, U. Shirwadkar, and K. S. Shah, Selected properties of $Cs_2LiYCl_6$, $Cs_2LiLaCl_6$, and $Cs_2LiLaYBr_6$ scintillators, IEEE Trans. Nucl. Sci. **58**, 333 (2011).

[27] M.-H. Du, K. Biswas, and D. J. Singh, in *Proceedings of SPIE 8507, Hard X-Ray, Gamma-Ray, and Neutron Detector Physics XIV* (SPIE, San Diego, 2012), p. 850705.

[28] E. V. Loef, P. Dorenbos, C. v. Eijk, K. Kramer, and H. Gudel, Scintillation and spectroscopy of the pure and Ce doped $Cs_2LiYX_6$, J. Phys. Condens. Matter **14**, 8481 (2002).

[29] A. Bessiere, P. Dorenbos, C. W. E. van Eijk, K. W. Kramer, H. U. Gudel, and A. Galtayries, Scintillation and anomalous emission in elpasolite $Cs_2LiLaCl_6:Ce^{3+}$, J. Lumin. **117**, 187 (2006).

[30] J. K. Cheon, S. Kim, G. Rooh, J. H. So, H. J. Kim, and H. Park, Scintillation characteristics of $Cs_2LiCeBr_6$ crystal, Nucl. Instrum. Methods Phys. Res., Sect. A **652**, 205 (2011).

[31] S. Kim, J. Moon, H. J. Kim, H. Park, H. Kang, S. H. Doh, D. Kim, and S. J. Kang, Scintillation properties of a $Cs_2LiCeBr_6$ crystal under X-ray, gamma-ray and proton irradiations, J. Korean Phys. Soc. **54**, 2098 (2009).

[32] G. Rooh, H. J. Kim, H. Park, and S. Kim, Luminescence and scintillation characterization of $Cs_2NaGdBr_6:Ce^{3+}$ single crystal, J. Lumin. **132**, 713 (2012).

[33] J. Glodo, E. V. D. van Loef, W. M. Higgins, and K. S. Shah, in *Proceedings of the 2006 IEEE Nuclear Science Symposium and Medical Imaging Conference* (IEEE, New York, 2006), p. 1208.

[34] U. Shirwadkar, J. Glodo, E. V. van Loef, R. Hawrami, S. Mukhopadhyay, A. Churilov, W. M. Higgins, and K. S. Shah, Scintillation properties of $Cs_2LiLaBr_6$ (CLLB) crystals with varying $Ce^{3+}$ concentration, Nucl. Instrum. Methods Phys. Res., Sect. A **652**, 268 (2011).

[35] H. Shi and M.-H. Du, Discrete Electronic Bands in Semiconductors and Insulators: Potential High-Light-Yield Scintillators, Phys. Rev. Applied **3**, 054005 (2015).

[36] X. W. Zhou and F. P. Doty, Embedded-ion method: An analytical energy-conserving charge-transfer interatomic potential and its application to the La-Br system, Phys. Rev. B **78**, 224307 (2008).

[37] H. Wei, L. Stand, M. Zhuravleva, F. Meng, V. Martin, and C. L. Melcher, Two new cerium-doped mixed-anion elpasolite scintillators: $Cs_2NaYBr_3I_3$ and $Cs_2NaLaBr_3I_3$, Opt. Mater. **38**, 154 (2014).

[38] H. Wei, M. Zhuravleva, M. Tyagi, and C. L. Melcher, Scintillation properties of $Cs_3LaCl_6:Ce^{3+}$ and $Cs_3LaBr_6:Ce^{3+}$, IEEE Trans. Nucl. Sci. **61**, 390 (2014).

[39] H. Wei, V. Martin, A. Lindsey, M. Zhuravleva, and C. L. Melcher, The scintillation properties of $CeBr_{3-x}Cl_x$ single crystals, J. Lumin. **156**, 175 (2014).

[40] H. Wei, M. Zhuravleva, F. Meng, and C. L. Melcher, Temperature dependence spectroscopic study of Ce-doped $Cs_3LaCl_6$ and $Cs_3LaBr_6$ scintillators, J. Lumin. **160**, 64 (2015).

[41] K. Momma and F. Izumi, VESTA 3 for three-dimensional visualization of crystal, volumetric and morphology data, J. Appl. Crystallogr. **44**, 1272 (2011).

[42] S. B. Donnald, M. Tyagi, H. E. Rothfuss, J. P. Hayward, M. Koschan, M. Zhuravleva, M. Fang, and C. L. Melcher, Sample-to-sample variation in single crystal YAP:Ce non-proportionality, IEEE Trans. Nucl. Sci. **61**, 332 (2014).

[43] L. M. Bollinger and G. E. Thomas, Measurement of the time dependence of scintillation intensity by a delayed-coincidence method, Rev. Sci. Instrum. **32**, 6 (1961).

[44] H. Wei, M. Zhuravleva, K. Yang, B. Blalock, and C. L. Melcher, Effect of Ba substitution in $CsSrI_3:Eu^{2+}$, J. Cryst. Growth **384**, 27 (2013).

[45] G. Kresse and D. Joubert, From ultrasoft pseudopotentials to the projector augmented-wave method, Phys. Rev. B **59**, 1758 (1999).

[46] G. Kresse and J. Furthmuller, Efficient iterative schemes for ab initio total-energy calculations using a plane-wave basis set, Phys. Rev. B **54**, 11169 (1996).

[47] G. Jomard, T. Petit, A. Pasturel, L. Magaud, G. Kresse, and J. Hafner, First-principles calculations to describe zirconia pseudopolymorphs, Phys. Rev. B **59**, 4044 (1999).

[48] J. Paier, M. Marsman, K. Hummer, G. Kresse, I. C. Gerber, and J. G. Angyan, Screened hybrid density functionals applied to solids, J. Chem. Phys. **124**, 154709 (2006).

[49] K. Biswas and M. H. Du, First principles study of native defects in InI, J. Appl. Phys. **109**, 113518 (2011).

[50] M. H. Du, First-principles study of native defects in TlBr: Carrier trapping, compensation, and polarization phenomenon, J. Appl. Phys. **108**, 053506 (2010).

[51] M. H. Du and S. B. Zhang, Impurity-bound small polarons in ZnO: Hybrid density functional calculations, Phys. Rev. B **80**, 115217 (2009).

[52] M. Gajdoš, K. Hummer, G. Kresse, J. Furthmüller, and F. Bechstedt, Linear optical properties in the projector-augmented wave methodology, Phys. Rev. B **73**, 045112 (2006).

[53] P. E. Blöchl, Projector augmented-wave method, Phys. Rev. B **50**, 17953 (1994).

[54] M. D. Birowosuto, P. Dorenbos, C. W. E. van Eijk, K. W. Kramer, and H. U. Gudel, Scintillation properties and anomalous $Ce^{3+}$ emission of $Cs_2NaREBr_6:Ce^{3+}$ (RE = La, Y, Lu), J. Phys. Condens. Matter **18**, 6133 (2006).

[55] See Supplemental Material at http://link.aps.org/supplemental/10.1103/PhysRevApplied.5.024008 for the optical band gap determination, absorption and transmittance spectra, PL emission of $Cs_2NaLaBr_3I_3$ at RT without normalization, scintillation rise time, and the temperature-dependent PL emission intensity of the extrinsic samples.

[56] P. Dorenbos, E. V. D. van Loef, A. P. Vink, E. van der Kolk, C. W. E. van Eijk, K. W. Kramer, H. U. Gudel, W. M. Higgins, and K. S. Shah, Level location and spectroscopy of $Ce^{3+}$, $Pr^{3+}$, $Er^{3+}$, and $Eu^{2+}$ in $LaBr_3$, J. Lumin. **117**, 147 (2006).

[57] E. Zych and J. Trojan-Piegza, Low-temperature luminescence of $Lu_2O_3:Eu$ ceramics upon excitation with synchrotron radiation in the vicinity of band gap energy, Chem. Mater. **18**, 2194 (2006).

[58] J. C. van't Spijker, *Luminescence and Scintillation of $Ce^{3+}$ Doped Inorganic Materials for Gamma-Ray Detection* (Delft University Press, Delft, 1999).

[59] A. L. Shluger and A. M. Stoneham, Small polarons in real crystals—Concepts and problems, J. Phys. Condens. Matter **5**, 3049 (1993).

[60] A. M. Stoneham, J. Gavartin, A. L. Shluger, A. V. Kimmel, D. M. Ramo, H. M. Ronnow, G. Aeppli, and C. Renner, Trapping, self-trapping and the polaron family, J. Phys. Condens. Matter **19**, 255208 (2007).

[61] M. D. Birowosuto, P. Dorenbos, J. T. M. de Haas, C. W. E. van Eijk, K. W. Kramer, and H. U. Gudel, Li-based thermal neutron scintillator research; $Rb_2LiYBr_6:Ce^{3+}$ and other elpasolites, IEEE Trans. Nucl. Sci. **55**, 1152 (2008).

[62] M. Moszynski, M. Kapusta, D. Wolski, and W. Klamra, Properties of the YAP: Ce scintillator, Nucl. Instrum. Methods Phys. Res., Sect. A **404**, 157 (1998).

[63] K. Biswas and M. H. Du, Energy transport and scintillation of cerium-doped elpasolite $Cs_2LiYCl_6$: Hybrid density functional calculations, Phys. Rev. B **86**, 014102 (2012).

[64] M. H. Du and K. Biswas, Electronic structure engineering of elpasolites: Case of $Cs_2AgYCl_6$, J. Lumin. **143**, 710 (2013).